PERGAMON

International Journal of Solids and Structures 36 (1999) 2557–2583

INTERNATIONAL JOURNAL OF SOLIDS and STRUCTURES

Validation and internal length scale determination for a gradient damage model: application to short glass-fibre-reinforced polypropylene

M. G. D. Geers[a,c,*], R. de Borst[b,c], W. A. M. Brekelmans[c], R. H. J. Peerlings[c]

[a] *Faculty of Civil Engineering, Royal Military Academy, Avenue Renaissance 30, B-1000 Brussels, Belgium*
[b] *Faculty of Civil Engineering, Delft University of Technology, P.O. Box 5048, 2600 GA Delft, The Netherlands*
[c] *Faculty of Mechanical Engineering, Eindhoven University of Technology, P.O. Box 513, 5600 MB Eindhoven, The Netherlands*

Received 21 May 1997; in final form 16 March 1998

Abstract

A strain-based transient-gradient damage model is used to analyse and describe the experimentally observed failure process in a Compact-Tension test carried out on short glass-fibre-reinforced polypropylene. Several aspects regarding the nonlocal character of the damage process in the material are emphasized and the intrinsic length scale is determined using available strain fields from an experimental analysis. A good agreement between theory and experiments has been found on a global and on a local level.

1. Introduction

Nonlocal constitutive approaches provide an adequate solution for the ill-posedness of the rate boundary value problem which occurs in standard, rate-independent continuum models of failure processes (de Borst et al., 1993; de Borst et al., 1995). The nonlocal character of the damage evolution is inherent in the micromechanical processes that govern the failure phenomena. The experimental validation of nonlocal approaches can only be carried out with appropriate experimental setups in which either the micromechanical processes themselves or their effects on the local macroscopic material behaviour are quantified.

The present analysis has been carried out on short glass-fibre-reinforced polypropylene (SGFPP), which is commercialized for the construction of bumpers in the vehicle industry. The primary application of this material is thus of a protective kind, which makes a damage and failure analysis

* Corresponding author. Tel.: 0031 40 2475076; fax: 0031 40 2447355; e-mail: geers@wfw.wtb.tue.nl

0020–7683/99/$ - see front matter
PII: S0020–7683(98)00123–1

particularly meaningful. Consequently, the computational modelling of damage and fracture phenomena in these composite materials attracts more and more attention.

Interesting experiments on fibre-reinforced composite materials have been realized by Czigány et al. and Karger-Kocsis et al. (Czigány and Karger-Kocsis, 1993a; Czigány and Karger-Kocsis, 1993b; Karger-Kocsis, 1993; Karger-Kocsis and Fejes-Kozma, 1994; Karger-Kocsis et al., 1995). In these experiments, acoustic emission, light-microscopy and infrared thermography were used to register the failure events. Although qualitatively useful from a physical point of view, these experimental results do not provide quantitative information on the local strains in the composite material, and are therefore not suitable for a comparison with numerical simulations in which an internal length scale parameter has to be determined.

In this work, the Hentschel Random Access Tracking System (Zamzow, 1990) has been applied to measure displacements locally in the failure zone of SGFPP on Compact-Tension (CT) specimens (Geers et al., 1996b). Local strain fields can thus be obtained, which reveal the process zone where damage is accumulated, and which characterize the crack propagation and opening process in a quantitative manner. The resulting data can be used to fit numerical simulations to the physical reality. The experimental results are interpreted, using observations obtained from SEM-micrographs, in agreement with some phenomenological conclusions made by other authors (Hugo et al., 1993; Czigány and Karger-Kocsis, 1993a; Karger-Kocsis, 1993; Karger-Kocsis and Fejes-Kozma, 1994; Karger-Kocsis et al., 1995; Hine et al., 1996). Along with the registration of the local deformations, global load-displacement curves have been obtained in a classical way. In addition to the non-uniform CT-tests, standard tensile tests have been carried out in order to evaluate the elastic properties.

2. Experimental analysis of SGFPP

2.1. Experimental setup

The CT-test is a well-known standard test method for plane fracture of metals and for the measurement of fatigue crack growth rates. In this test the deformation is non-uniform, characterized by the presence of high deformation gradients in front of the notch of the specimen. The test, described in the ASTM Standards E399 and E647, has been adapted to the particular requirements imposed by composite materials (Williams and Cawood, 1990). As the thickness of the available SGFPP-plates is small compared to the in-plane dimensions, the specimens are supposed to be subjected to plane-stress conditions.

The test specimen is a single edge-notched plate. The general proportions of this specimen are shown in Fig. 1, while a cracked SGFPP CT-specimen is depicted in Fig. 2.

The principle parameters that identify a CT-specimen are the characteristic dimension W and the notch depth a_n (Fig. 1). The CT-specimens used in the current experiments were mechanically cut out of SGFPP-plates (Azdel® PD3243 Radlite) with a thickness of 3.8 mm, kindly provided by GE Plastics Europe. Straight notches were manufactured by milling. The characteristic dimension W of the specimens used in the present study is 50 mm or 75 mm, since for these specimen sizes disturbing out-of-plane deformations are not triggered. Various test conditions were realized by using different notch depths and different loading rates for each specimen size. Measurements

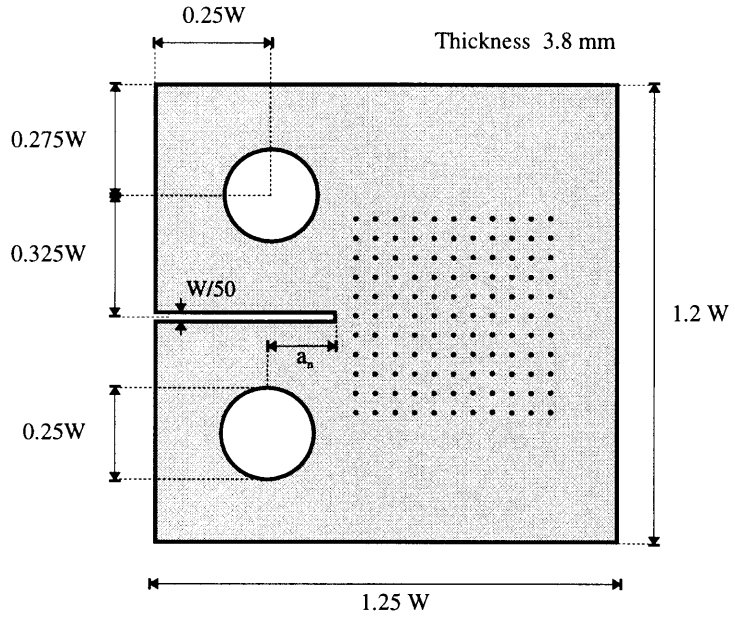

Fig. 1. The Compact-Tension specimen.

were performed both dynamically (continuous increase of the deformations) and statically (stepwise increase of the deformations). All experiments have been carried out at room temperature.

The glass-fibre content of the SGFPP-plates was 30 wt%, with an average fibre length of approximately 12.5 mm, randomly distributed in the matrix. All specimens were tested perpendicular to the rolling direction since the SGFPP-plates may show a preferential fibre orientation in the rolling direction due to the drying, heating, consolidation and cooling in the paper-making route for the production of the material (Gibson and Manson, 1992). Nevertheless, the material is expected to behave in an isotropic manner.

The measurement of the displacement fields has been carried out with the optical particle tracking system from Hentschel (Zamzow, 1990; Geers et al., 1996b). Displacements were measured on a quasi-square grid of 121 optical markers attached to the specimen in front of the notch. These optical markers can be observed on the photographical representation of the cracked specimen in Fig. 2. From these displacement fields, strain fields have been computed using a higher-order strain derivation technique (Geers et al., 1996a).

It should be remarked that classical tensile tests are very difficult to use in order to examine all aspects of the failure process of quasi-brittle materials. The deformation in such a test remains uniform and elastic until a critical strain is reached at which damage starts to localize in a narrow zone of the specimen. At this point, uniformity of the damage distribution is lost and direct identification procedures based on global deformation characteristics are no longer possible. For this specific material, the situation is even worse, since an unstable behaviour occurs. This instability is accompanied by snap-back due to the sudden release of elastically stored energy, which cannot be traced without a servo-controlled load mechanism. Rupture occurs suddenly, even for short

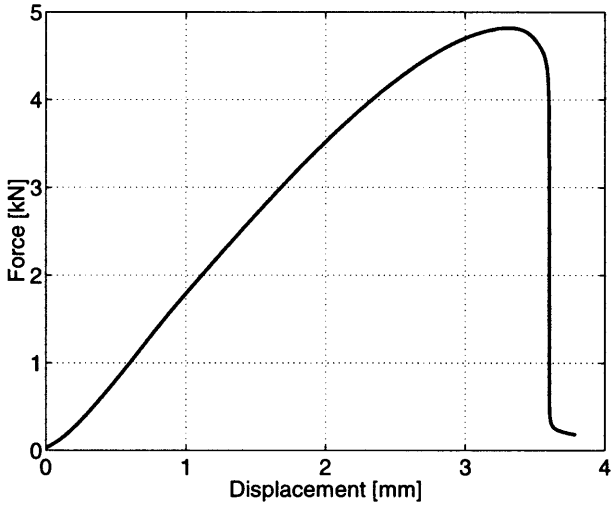

Fig. 3. Brittle rupture in a classical tensile test.

bar lengths. A typical force-displacement curve for a tensile test is shown in Fig. 3, where the falling branch is unstable.

2.2. Phenomenological aspects of the failure process

The nonlocal character of the failure behaviour of SGFPP can be easily understood by examining the failure mechanisms. These mechanisms consist of a sequence of matrix deformation, matrix cracking, fibre-matrix debonding and fibre pull-out. The fibre-matrix debonding and the fibre pull-out phenomena are clearly illustrated in Fig. 4. The small holes after the pull-out and the lateral debonding at the fracture surface can be observed well.

Fibre-matrix debonding and fibre pull-out are characterized by significant displacements and thus by high strains. In a CT-test, damage and failure develop progressively through the specimen. After the test, the two parts of the specimen are not fully separated since the fibre pull-out has not been completed. Fibre fracture, which is a dominant failure event in long glass-fibre-reinforced polypropylene, has also been observed as a secondary failure mechanism.

An essential difficulty in modelling the mechanical behaviour of composites is the crack bridging by fibres, which is a macroscopically continuous process. A micrograph of the fibre pull-out and the bridging effects in the crack zone of SGFPP is shown in Fig. 5. A clear view of the crack propagation and opening process is given in Fig. 6 which has been taken after the completion of the experiment. The fibre pull-out and the fibre bridging mechanisms are obvious.

The failure mechanisms described above are clearly spatially nonlocal on the mesolevel. In this case the fibres dominate the long range effects on the macroscopic level, which is characteristic for all nonlocal approaches of damage and fracture (either at the micro-level at the meso-level or at the macro-level).

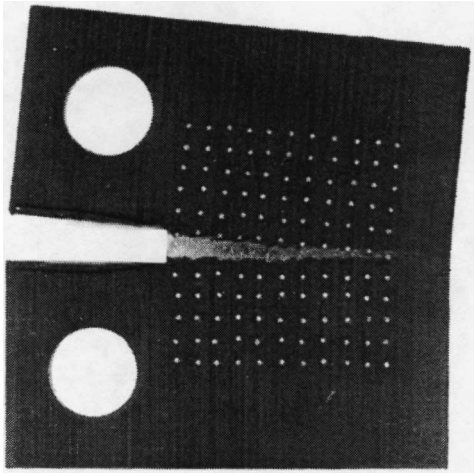

Fig. 2. A fully cracked CT-specimen.

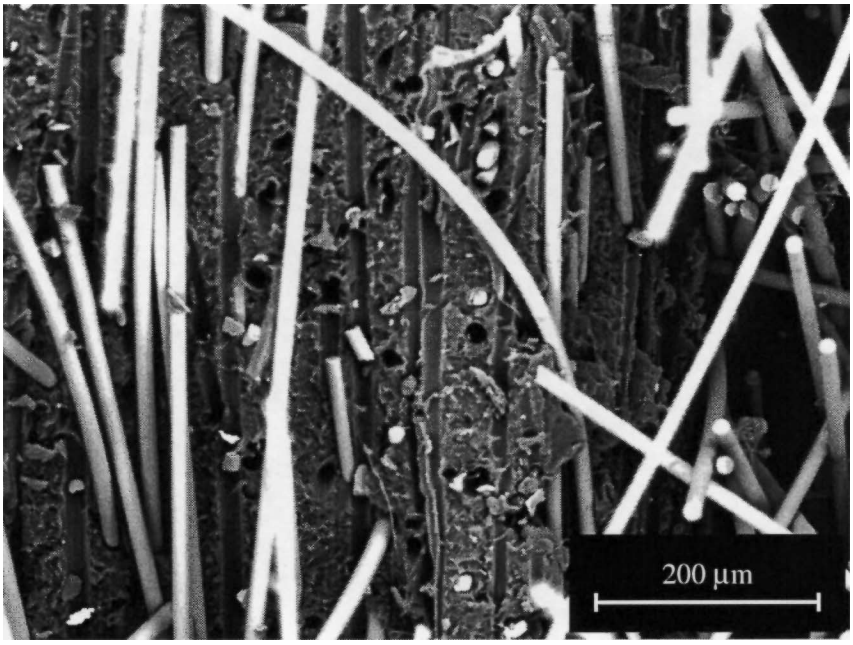

Fig. 4. Fibre-matrix debonding and fibre pull-out in SGFPP.

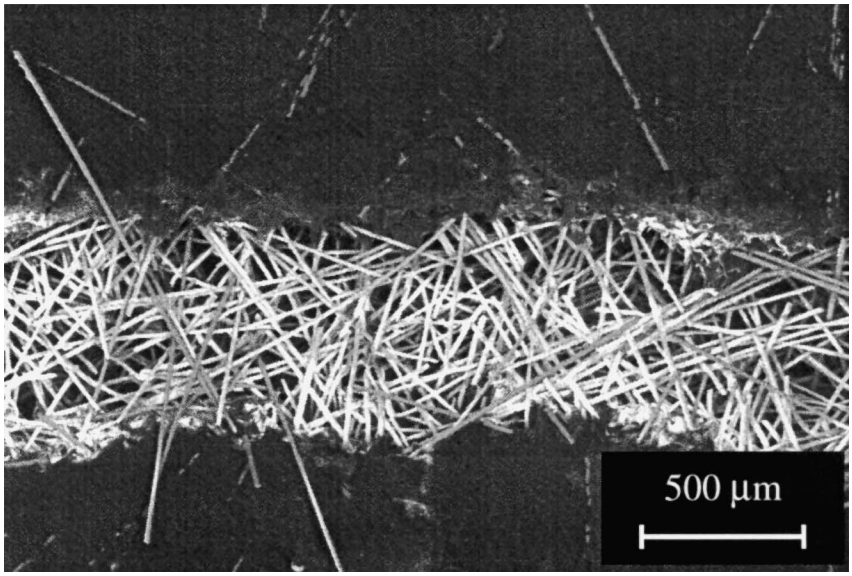

Fig. 5. Fibre bridging in the crack zone.

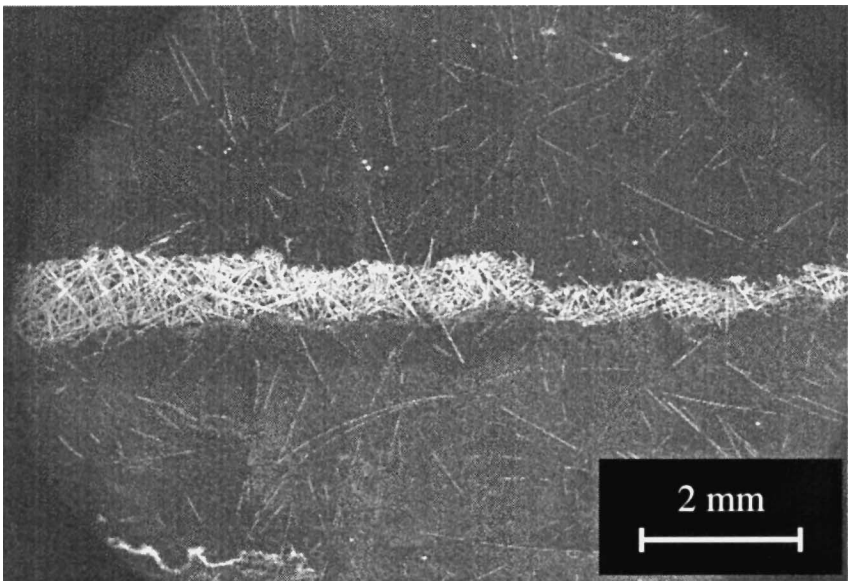

Fig. 6. Crack growth in SGFPP.

2.3. Experimental results

The experimental analysis (Geers et al., 1996b; Geers, 1997) has shown that the reproducibility of the experiments is acceptable and that no significant rate-dependence exists within the accuracy and the reproducibility of the experiments. Measurements of some basic elastic material characteristics using classical tensile tests has led to a Poisson's ratio v equal to 0.28 and a damage initiation value κ_i of the strain that equals 1.1%. Young's modulus E in the CT-test was found to be equal to 3200 MPa, which is close to the modulus of the polypropylene matrix material.

Strain fields have been determined during the CT-tests, which permits the examination of the evolution of the process zone in front of the crack tip. The results can be visualized at different loading steps. Most of these tests gave reliable and reproducible results, which makes it possible to limit the discussion to representative data reflecting the common conclusions of all tests. Figure 7 gives a three-dimensional view of the ε_{yy}-component of the strain (in the load direction), while Fig. 8 shows the positioning of the strain field on the specimen. The computed strain field (initial loading phase) is depicted over the entire marker field of the CT-specimen. The localization zone in front of the notch is located within the process zone where damage is built up.

During the entire loading process, strains have also been derived from displacements over the crack that splits the specimen progressively. These strains will be referred to as fictive strains. The use of such fictive strains can be justified in continuum damage mechanics, where the cracks are treated as fully damaged but continuous material. The numerical values computed for these fictive strains may be large, and can easily exceed 100% in the final failure stage. In a continuous strain field, a threshold value exists beyond which the computed strain can no longer be considered as a relative measure of material elongation. The fictive strains exceeding this threshold value are essential characteristics of a physical crack and they are directly related to the crack opening displacements. These fictive strains are reproducible and only valid on the specific discretization pattern that has been used. The actual value of the fictive strains fully depends on the discretization distance between the measurement points. If the same pattern of the measurement points is

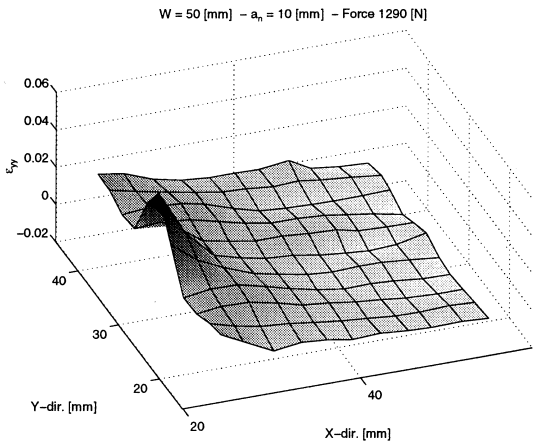

Fig. 7. ε_{yy} strain field on marker grid.

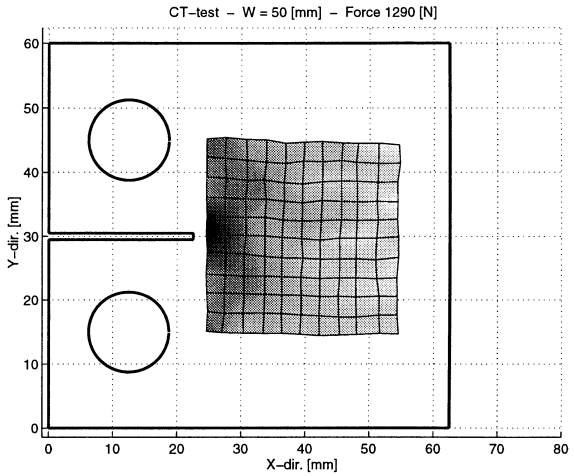

Fig. 8. ε_{yy} strain field in projection.

considered in the numerical model which will be discussed next, a comparative analysis becomes possible.

The CT-tests that were performed provide global (load-displacement) data and local (displacement fields and strain fields) data which can be used to estimate the parameters in a constitutive model including the length parameter in higher-order continuum descriptions. Classically, most fitting procedures are limited to global results, which may lead to erroneous conclusions. In the particular case of short glass-fibre-reinforced polypropylene, the present local measurements on the CT-specimens permit the assessment of numerical models.

3. Numerical model

The numerical modelling of the failure behaviour will be carried out with a spatially non-local constitutive model. The determination of all the characteristic parameters which influence this numerical process is not easy. So far, no experimental tests exist which permit the determination of each of these parameters in a unique way. Suggestions for the measurement of the characteristic length of a nonlocal continuum were made by Bažant and Pijaudier-Cabot (1989, 1995), by de Borst et al. (1997a, 1997b) and by Carmeliet (1997). However, the definition of the characteristic length is not unambiguous and depends on the constitutive framework in which it is embedded. Specific experimental procedures and methods have to be set up in agreement with the physical phenomena which govern the localization and fracture process. The necessary data have to be extracted from complex tests, combined with an iterative procedure based on a proper understanding of the significant and influence of each parameter.

The analysed material (SGFPP) presents a rather complex behaviour, which renders the validation process of a numerical model difficult. Isotropy and an average linear elastic behaviour below the damage threshold are assumed. The primary goal of the present simulations is to validate

the applicability of the strain-based transient-gradient damage method summarized below (Geers, 1997; Geers et al., 1998), and to estimate all material parameters in the case of a CT-test.

3.1. Strain-based transient-gradient damage

For the modelling of the short glass-fibre-reinforced polypropylene we shall use the framework of damage mechanics. In particular, we shall use an isotropic strain-based damage formulation enriched with gradient terms (Peerlings et al., 1996a) for which an in-depth dispersion analysis has been presented by Peerlings et al. (1996b). Similar lines have been pursued by Frémond and Nedjar (1996) and Mühlhaus et al. (1994). The special feature of the theory used here is that the extent in which gradient terms play a role is directly linked to the local strain state: for increasing local strains the nonlocal interaction and thus the gradient terms become more important. The theory as well as its numerical elaboration are given in full detail by Geers (1997) and Geers et al. (1998). For completeness the basic structure of the model is briefly summarized below.

Isotropic elastic strain-based damage formulations are normally rooted in a total stress-strain relation:

$$\sigma = (1-D)^4 C : \varepsilon \tag{1}$$

with σ the Cauchy stress tensor, ε the infinitesimal strain tensor, ${}^4C$ the fourth-order elastic stiffness tensor and D the scalar-valued damage variable, such that

$$0 \leqslant D \leqslant 1 \tag{2}$$

The damage parameter (1) is coupled to the deformation history of the material through the use of a monotonically increasing deformation history parameter κ. This scalar history parameter characterizes the ultimate deformation that the material has experienced in its loading history. The value of the actual history parameter at time t is determined from the evolution of a damage equivalent strain. Local damage models use a local damage equivalent strain, denoted by e, which can be mathematically derived from the different strain components of the local strain tensor. The definition for the equivalent strain e mainly influences the sensitivity of the failure process with respect to the different principal strain components. The present definition of e is based on the positive principal strain components ε_j^+ (Mazars and Pijaudier-Cabot, 1989):

$$e = \sqrt{\sum_{j=1,2,3} (\varepsilon_j^+)^2} \tag{3}$$

If a markable difference exists between the compressive and tensile behaviour of a material, the selected formulation should reflect this, e.g. for concrete (Peerlings et al., 1997). The failure behaviour in a CT-test is mode-I dominant and fracture is initiated through the exhaustion of the tensile resistance of the material. The threshold value for compression failure is significantly higher than the threshold value for tension, and this failure mode is not mobilized in the experiment.

The incorporation of the nonlocal effect requires the computation of a nonlocal equivalent strain, denoted by $\bar{e}$, which characterizes the deformation in a material volume surrounding a point. The nonlocal effect reflects the spatial interaction of neighbouring material elements at the micro-level. If the vector $\vec{x}$ characterizes the present position of the point of consideration, and $\vec{\xi}$

the relative positions of the material points in a surrounding volume V, then one may write at time t: $D(\vec{x}, t) = D(\kappa(\vec{x}, t))$, where the history parameter κ is defined by

$$\kappa(\vec{x}, t) = \max\left[(\epsilon(\vec{x}, \tau)|\tau \leqslant t), \kappa_i\right] \tag{4}$$

for local damage models and

$$\kappa(\vec{x}, t) = \max\left[(\bar{\epsilon}(\vec{x}, \tau) = \bar{\epsilon}(\epsilon(\vec{\xi}, \tau)|\vec{\xi} \in V(\vec{x}))|\tau \leqslant t), \kappa_i\right] \tag{5}$$

for nonlocal damage models. The threshold value for damage initiation κ_i is the initial value for κ at time $t = 0$, which is the ultimate equivalent strain that characterizes the elastic material behaviour prior to occurrence of damage. Alternatively, the evolution of κ defined by eqn (5) can be mathematically expressed by the Kuhn-Tucker relations

$$\dot{\kappa} \geqslant 0, \quad \bar{\epsilon} - \kappa \leqslant 0, \quad \dot{\kappa}(\bar{\epsilon} - \kappa) = 0 \tag{6}$$

The damage parameter D progressively reduces the stiffness of the material in the sense of Kachanov (Kachanov, 1958). The damage evolution law governs the failure behaviour of the material. The parameters in the damage evolution law must provide the necessary flexibility to model the mechanical response of the material. The used damage evolution law is a power law, defined by

$$D = 1 - \left[\frac{\kappa_i}{\kappa}\right]^{\beta}\left(\frac{\kappa_c - \kappa}{\kappa_c - \kappa_i}\right)^{\alpha} \tag{7}$$

The critical history parameter κ_c characterizes the value of κ for which the damage D reaches its ultimate value 1. The exponents α and β influence the slope and the shape of the stress-strain softening curve (Geers, 1997). The damage threshold value κ_i mainly influences the peak of the load-displacement curve. In the case of SGFPP, crack bridging and fibre pull-out require a relatively large value of κ_c. A larger value of α progressively reduces the stresses during softening. The fine-tuning of the response has to be performed with β.

Peerlings et al. (1996) have proposed to link the nonlocal equivalent strain $\bar{\epsilon}$ to the local equivalent strain ϵ via

$$\bar{\epsilon} - c\nabla^2\bar{\epsilon} = \epsilon \tag{8}$$

Geers (1997) and Geers et al. (1998) have shown that this formulation, in which c is an additional material parameter with the dimension of length squared, is deficient in the sense that for progressive damage an artificial spreading of the damage zone orthogonal to the direction of crack propagation occurs. As a remedy, they have suggested to replace the constant c by a variable ζ, which will henceforth be referred to as the gradient activity. Now, eqn (8) which governs the evolution of the nonlocal equivalent strain, changes into

$$\bar{\epsilon} - \zeta\nabla^2\bar{\epsilon} = \epsilon \tag{9}$$

An additional evolution law now has to be specified, namely for the gradient activity ζ in eqn (9), which controls the nonlocal effect:

$$\zeta = \begin{cases} c\left(\frac{\epsilon}{\epsilon_\zeta}\right)^{n_\zeta} & \text{if } \epsilon \leqslant \epsilon_\zeta \\ c & \text{if } \epsilon > \epsilon_\zeta \end{cases} \tag{10}$$

The gradient activity ζ is limited to a maximum value c which is reached at the equivalent strain e_ζ. This expression has been tested for different values of e_ζ and n_ζ. It appeared that the influence of these parameters on the mechanical response is rather limited. Evolution law (10) has therefore been used in its linear form, by taking $n_\zeta = 1$. The value of e_ζ must be between κ_i and κ_c. The material characteristic value of the gradient parameter c must be in accordance with the physical nature of the nonlocal effect. This parameter controls the maximum width of the localization zone and the damage zone in a material. The gradient parameter c is the square of the length parameter that characterizes the nonlocal effect. The extent of the nonlocal effect decreases exponentially with the distance and a ratio of 5–10 between the maximum distance and $\sqrt{c}$ is realistic. For SGFPP, this means that a value of c between 1 mm^2 and 5 mm^2 should result. The adaptation of a first estimate is carried out by a comparative study of the global numerical-experiment results and of the associated local strain fields.

3.2. The finite element model of the CT-test

The application of the finite element method for the analysis of a CT-test requires an appropriate meshing of the specimen and the loading pins. Three meshes have been generated for the specimens (Figs 9–11). The meshes have been refined progressively in the band where the crack is expected, in order to investigate the possible mesh dependence of the numerical results. The additional refinement in the vicinity of the notch for the coarse and medium mesh is necessary to model the correct shape and size of the small notch in the CT-specimen.

The loading pins have been modelled with elastic springs with a high rigidity in compression and zero stiffness in tension. This mechanical model of the loading pins ensures that no tensile forces can be transmitted to the edges of the holes and that the rotation of the specimen on the pins remains possible. The loading force is applied at the centre of the spring rosette, and the horizontal displacements of these loading centres are suppressed. The CT-specimen is meshed with nine-noded quadrilateral plane-stress elements and six-noded triangular elements, both with (bi)quadratic interpolation for the displacements and (bi)linear interpolation for the nonlocal

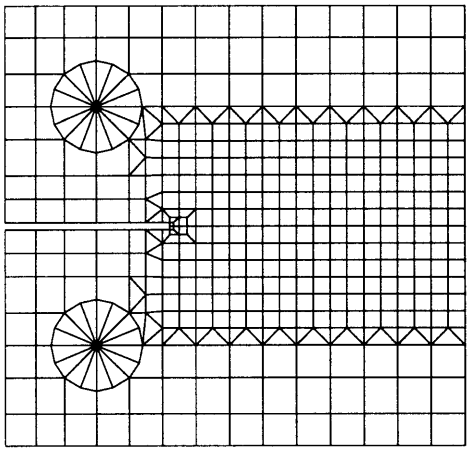

Fig. 9. Coarse mesh.

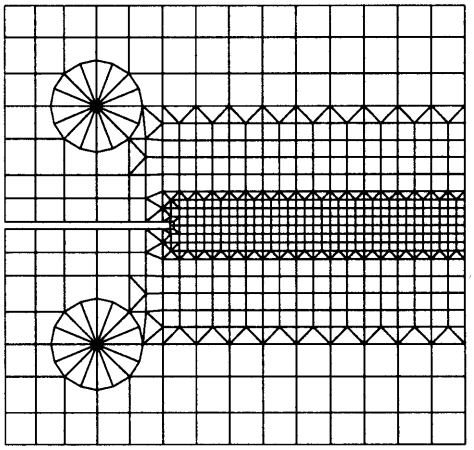

Fig. 10. Medium mesh.

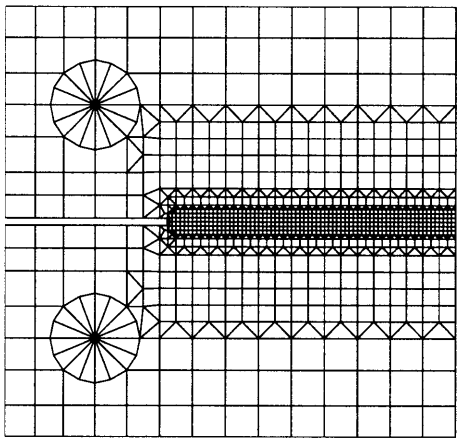

Fig. 11. Fine mesh.

equivalent strain $\bar{\varepsilon}$ and for the gradient activity ζ respectively (Geers, 1997; Geers et al., 1998). The symmetry properties of the specimen have been exploited in the computations, where only half the specimen is used with the appropriate boundary conditions. However, all results will be shown for the full specimen to facilitate the comparison with the experimental results.

4. Comparison of numerical and experimental results

4.1. Parameter quantification

The parameter estimation has been carried out on CT-specimens with a characteristic size $W = 50$ mm and a notch depth $a_n = 10$ mm (Fig. 1). The parameters obtained from the quanti-

Table 1
Parameter quantification for SGFPP on CT-experiments

Model parameters for SGFPP Quantity		Value	Units
Elastic material parameters			
Young's modulus	E	3200	MPa
Poisson's ratio	ν	0.28	
Nonlocal material parameters			
Evolution law ζ (10)	c	2	mm^2
	n_ζ	1	
	e_ζ	0.15	
Damage and failure parameters			
Damage evolution law (7)	κ_i	0.011	
	κ_c	0.5	
	α	5	
	β	0.75	

fication analysis based on the global mechanical response and the local strain fields are summarized in Table 1. With the exception of the parameters E, ν, κ_i, all parameters have been quantified by inverse modelling of the experiments.

4.2. Global and local comparison

The global comparison of the computational and experimental results is given in Fig. 12. The gray zone in this figure reflects the band which forms the envelope of the experimentally registered load-displacement curves. The displacement which has been used in these curves is the relative displacement of two well-defined reference points in the vicinity of the two outer markers, closest to the loading pins. Slip and secondary deformations in the clamps and the loading heads of the tensile machine are thus excluded from the comparative analysis. A bilinear interpolation was used to determine the actual experimental displacement of the reference point from the surrounding markers. The displacement in the abscissa of the computational curve is the same differential displacement as defined above, which is computed from the displacements of the reference points by interpolation on the nodal displacements in the corresponding elements. The computed response is superimposed on the experimental band, and fits well.

The numerical analysis of localization and failure phenomena is clearly dominated by the local and nonlocal material behaviour in the process zone. A parameter estimation procedure which does not take into account the experimental justification of local characteristics of the deformation process, is incomplete. The parameter values in Table 1 were determined by comparison of the computed and measured ε_{yy}-strain field for a CT-specimen with $W = 50$ mm and $a_n = 10$ mm. The strain fields used in this local comparative study are constructed on the same discretization pattern for both the experimental and the numerical results. The displacements of the numerical solution have been computed in all measurement points (or markers) using the element interpolation

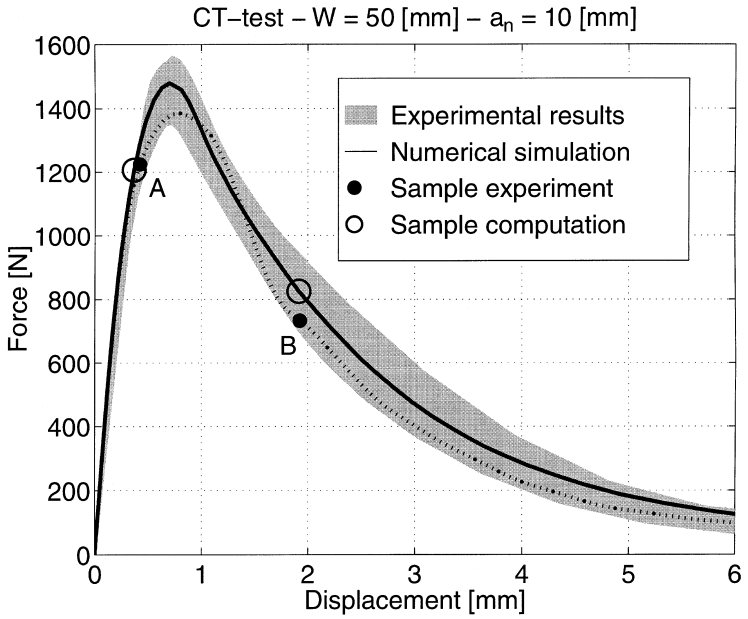

Fig. 12. Comparison of the mechanical responses for $W = 50$ mm and $a_n = 10$ mm.

functions and the nodal displacements of the numerical solution, and an objective quantitative comparison therefore becomes possible. Next, the strain fields have been constructed from the discrete displacement fields with a higher-order strain computation method (Geers et al., 1996a).

The local comparison has been carried out for two stages in the deformation process of the Compact-Tension specimen, as depicted in Fig. 12. The samples for these two stages have been selected from the global load-displacement curve of one single experiment and the corresponding curve of the computational result. Only a limited number of steps is available on each curve and the selected numerical sample is chosen as close as possible to the experimental sample. The samples A have been taken in the initial stage of damage accumulation and crack formation, while in the samples B crack propagation, crack opening and crack bridging have taken place.

The ε_{yy}-strain fields in the samples A are shown in a three-dimensional representation in Figs 13 and 14 with the experimental and computational results, respectively. These images permit a qualitative comparison of both strain fields. A more quantitative comparison can be carried out by projecting both strain fields on the $[X-\varepsilon_{yy}]$ plane. The representations in Figs 15 and 16 are thus obtained. The local numerical results approximate the measured strains in a satisfactory way. The peak strain is reasonably well predicted as well as the compressive zone at the right side of the specimen. The small oscillations in the experimental strain field observed in Figs 13 and 15 are due to measurement errors. It is emphasized that the experimental and the numerical samples do not exactly coincide on the global curve, which explains the small differences in strain amplitude.

A similar comparison is now made for samples B. The three-dimensional pictures of the ε_{yy}-strain fields are given in Figs 17 and 18. These figures compare the fictive strains computed from the crack opening rather than the physical strains in the material. Near sample B, Fig. 12 shows that the entire experimental curve lies under the computational curve. It can be noticed that the

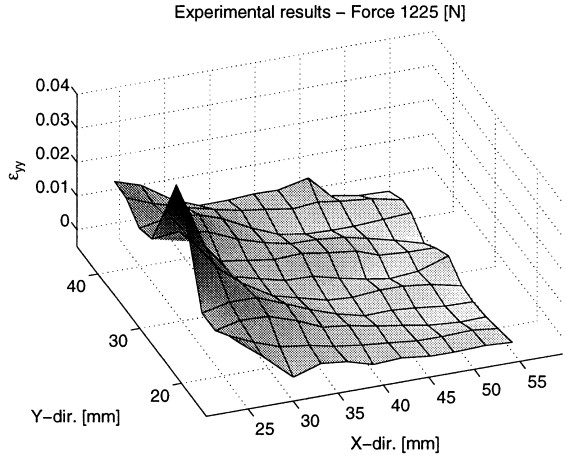

Fig. 13. Experimental ε_{yy}-strains, sample A.

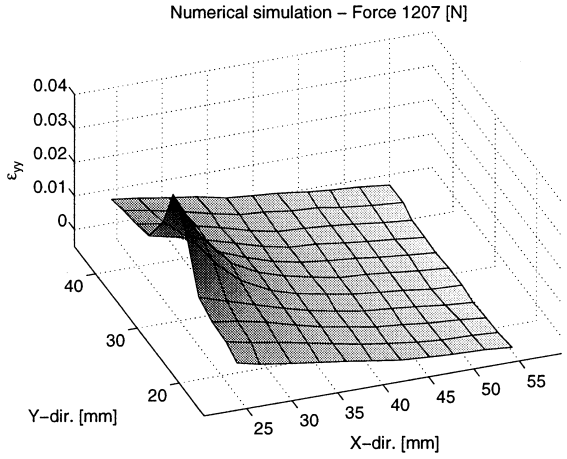

Fig. 14. Computational ε_{yy}-strains, sample A.

experimentally determined crack opening in Fig. 17 (e.g. for $X = 35$ mm) is larger than the computed crack opening in Fig. 18. On the other hand, Fig. 12 shows that the experimentally measured global displacement in sample B almost equals the computed value. The peak value of the strain in the experiment does not differ much from the peak value in the numerical simulation. The small overestimation of the loading force in the global softening path corresponds with a small underestimation of the crack opening between the specimen notch and the crack tip. However, these small differences may not obscure the good quality of the obtained agreement between experiment and computation. The comparison is made for only one experiment, and Fig. 12 reminds of the scatter between the different experiments. The experiment that was selected for the present local comparison has a post-peak behaviour situated in the lower region of the experimental band. Small differences between this single experiment and the computed result are therefore

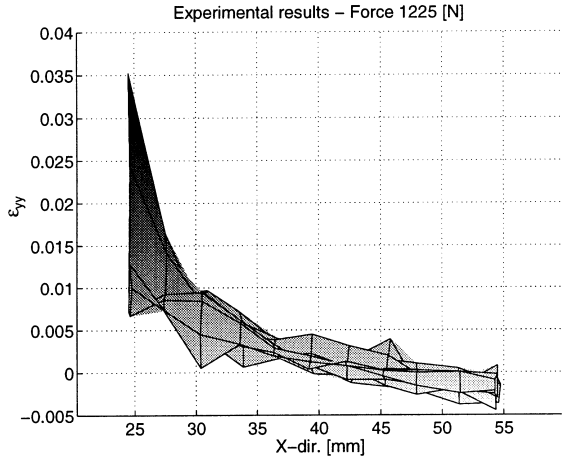

Fig. 15. Experimental ε_{yy}-strains, sample A.

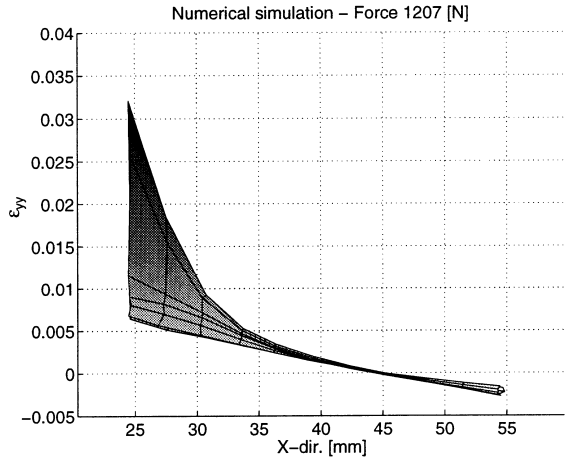

Fig. 16. Computational ε_{yy}-strains, sample A.

acceptable within the accuracy of the experimental technique that has been used. The numerical-experimental agreement may be considered as a validation of the theoretical and numerical description of the localization process and justifies the adopted failure parameters in the model.

4.3. Size and notch effects

An important issue in the present experimental verification is the reliable prediction of size effects and notch effects. Different specimen sizes with different notch depths have been examined experimentally. The numerical simulations of these experiments have been carried out with the *same* parameters as obtained from the $W = 50$ mm specimen with $a_n = 10$ mm (Table 1). The comparison of the computed and measured force-displacement curves is made in Fig. 19 for a

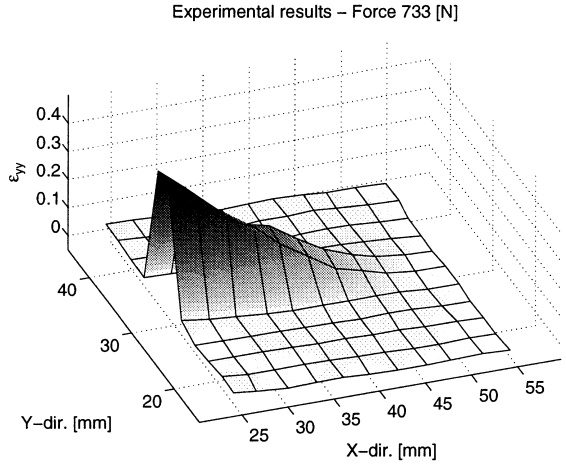

Fig. 17. Experimental ε_{yy}-strains, sample B.

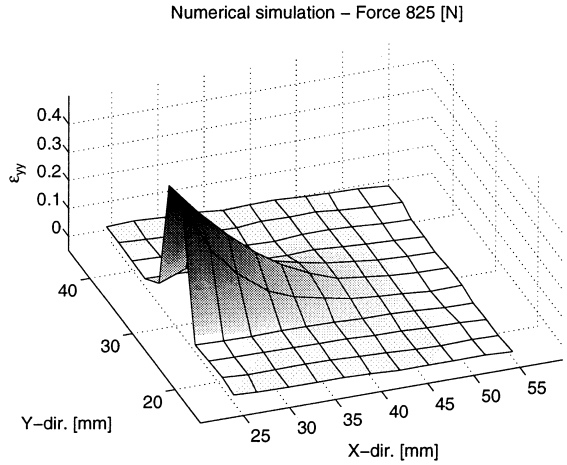

Fig. 18. Computational ε_{yy}-strains, sample B.

notch depth $a_n = 15$ mm. The peak behaviour is well predicted. The post-peak curve fits reasonably well, apart from the small underestimation in the larger displacement range.

In order to analyse the influence of the size effect, the specimens with $W = 50$ mm ($a_n = 10$ mm or $a_n = 15$ mm) have been scaled up by 50% to a characteristic dimension $W = 75$ mm (notch depths $a_n = 15$ mm or $a_n = 22.5$ mm, respectively). The results are shown in the Figs 20 and 21. Unfortunately, only one experimental load-displacement curve was available for $W = 75$ mm and a notch depth of 15 mm. All other experimental bands presented so far, contain at least four experimental curves. This lack of experimental information is due to out-of-plane displacements of the specimen combined with the loss of some critical marker signals which were necessary to retrieve the abscissa of the load-displacement curves. Nevertheless, the computed result depicted in Fig. 20 fits the experiment reasonably well. The small deviations in the post-peak behaviour

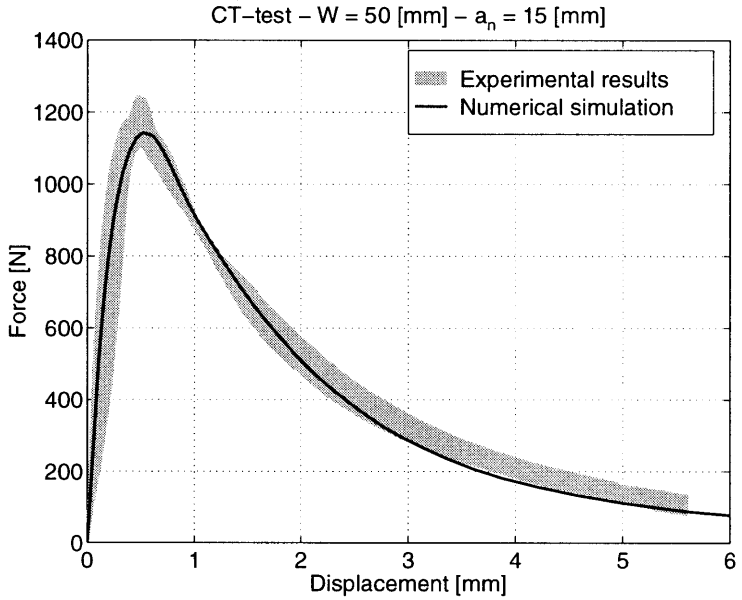

Fig. 19. Comparison of the mechanical responses for $W = 50$ mm and $a_n = 15$ mm.

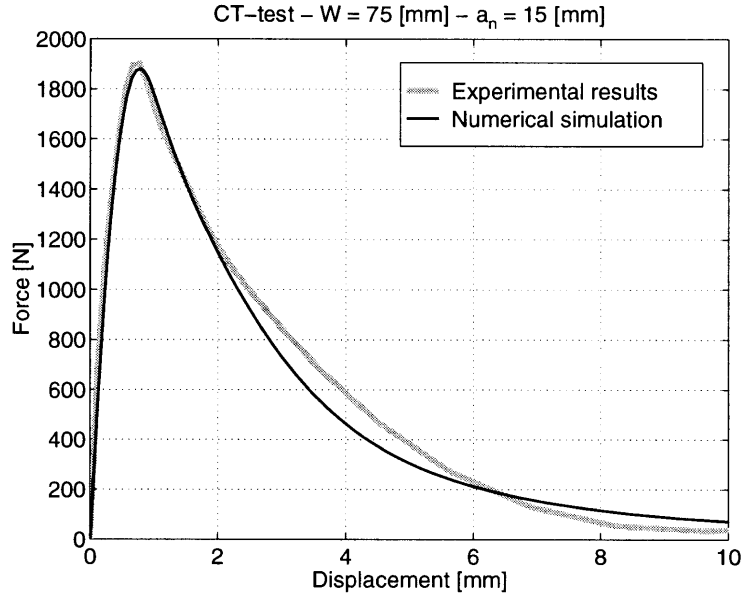

Fig. 20. Comparison of the mechanical responses for $W = 75$ mm and $a_n = 15$ mm.

cannot be interpreted adequately with a single experimental curve. By increasing the notch depth from 15 mm to 22.5 mm the maximum load and the post-peak response decrease significantly. The

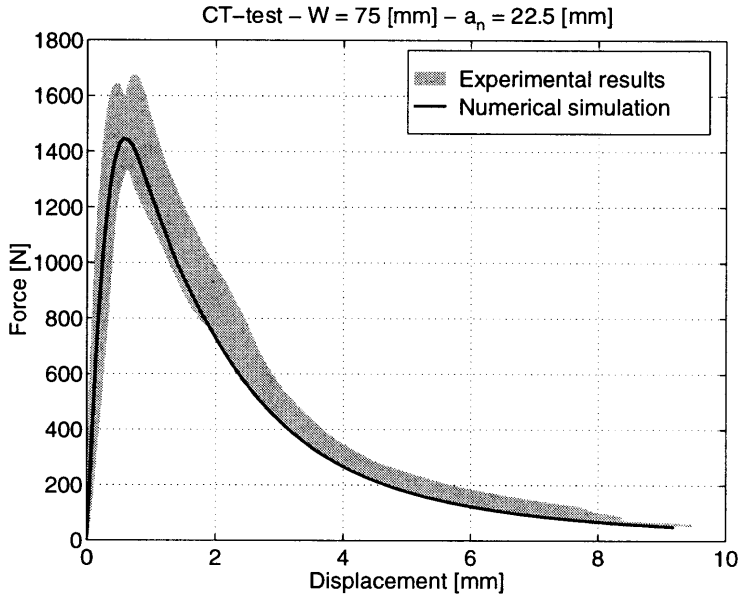

Fig. 21. Comparison of the mechanical responses for $W = 75$ mm and $a_n = 22.5$ mm.

computational prediction and the measured results are compared in Fig. 21. The prediction of the maximum loading force is good, while a small underestimation can be noticed in the descending branch. The analysis of size and notch effects proves that the present transient-gradient enhanced damage method properly describes the intrinsic mechanical processes which govern the global mechanical response.

4.4. On the necessity of local experimental verifications

The parameter quantification procedure has been carried out using global and local data. This section underlines the necessity of a local verification and shows that a correct parameter identification cannot be achieved without the consideration of the local behaviour. A parameter set will be presented which results in an acceptable global load-displacement response, but which fails when the numerical and experimental local strain fields are compared. In order to show this, a new parameter estimation process has been carried out with a different nonlocal material interaction. The inherent length parameter in this identification procedure is taken considerably higher than in the original parameter set, as a value of 100 mm^2 was adopted for the gradient parameter c. The identification process was carried out on the small CT-specimen ($W = 50$ mm and $a_n = 10$ mm) by fitting the global load-displacement behaviour only. Table 2 gives the set of parameters obtained for this analysis.

It is noticed that the increase of the nonlocal effect has been obtained by a higher gradient parameter and a smaller e_ζ in the gradient activity evolution law. The threshold value for the damage initiation κ_i has been decreased while the damage evolves more rapidly with respect to the history parameter κ. The global load-displacement curve is depicted in Fig. 22. The global response

Table 2
Incorrect material parameters for SGFPP on CT-experiments

Model parameters Quantity		Value	Units
Elastic material parameters (idem Table 1)			
Nonlocal material parameters			
Evolution law ζ (10)	c	100	mm^2
	n_ζ	1	
	e_ζ	0.05	
Damage and failure parameters			
Damage evolution law (7)	κ_i	0.008	
	κ_c	0.4	
	α	6	
	β	1	

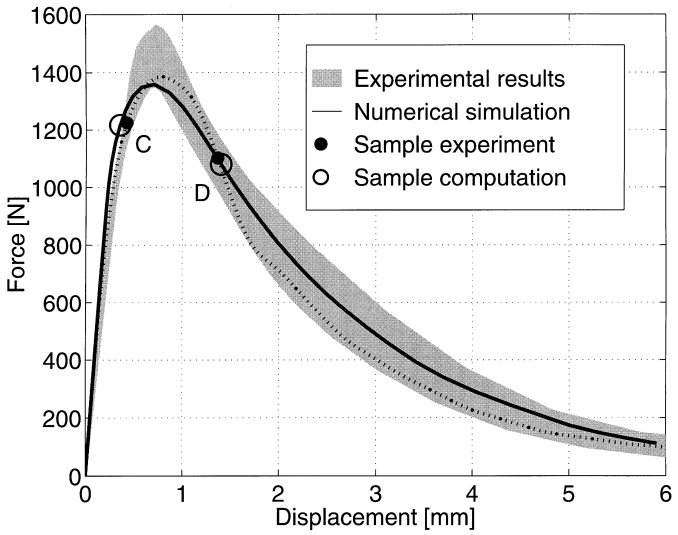

Fig. 22. Global verification and samples for the local verification.

fits the experimental results reasonably well. If no local analysis would have been carried out, this parameter set could have been accepted. However, different conclusions are drawn if the local behaviour is investigated. Two stages, denoted by C and D, are examined by taking appropriate samples on the load-displacement curve of Fig. 22. The local results in the samples of both stages will be compared next.

The three-dimensional representations of the ε_{yy}-strain fields in the samples C are compared in Fig. 23 (sample C on the experimental curve coincides with sample A) and Fig. 23. These images clearly reveal the differences between the simulation and the experiment. The peak value of the ε_{yy}-

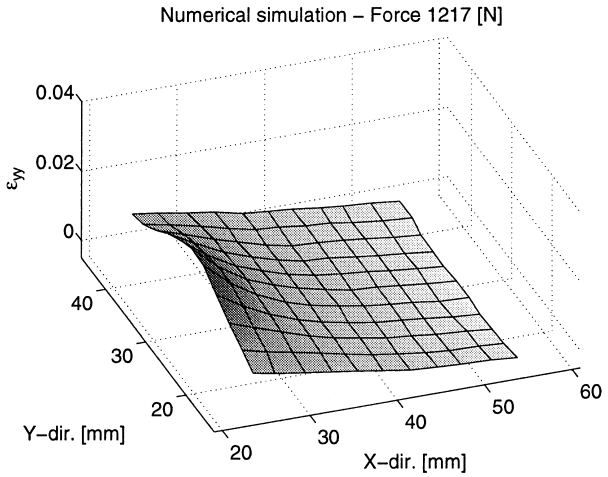

Fig. 23. Computational ε_{yy}-strains, sample C.

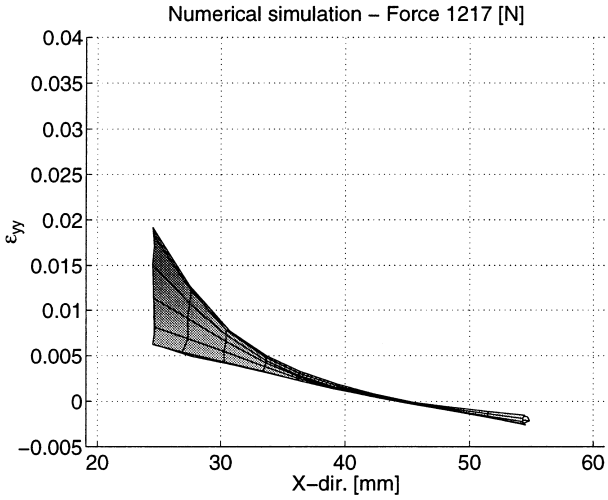

Fig. 24. Computational ε_{yy}-strains, sample C.

strain component in the simulation is much smaller than in the experiment and the strains are dispersed over a larger zone. A better quantitative comparison is obtained by projecting both strain fields on the $[X-\varepsilon_{yy}]$ plane as in Figs 15 and 24. This projection emphasizes the depth of the process zone and the behaviour in the compressive area of the specimen. The comparison in sample C is made during the initial build-up of the process zone which results in the onset of the crack propagation. It can be noticed from Figs 15 and 24 that the error is large in the process zone close to the crack tip and considerably smaller in the compressive zone. This observation is in agreement with the fact that the nonlocal effect only influences the process zone where the failure is initiated.

The samples of stage D are located on the structural softening path. The three-dimensional ε_{yy}-

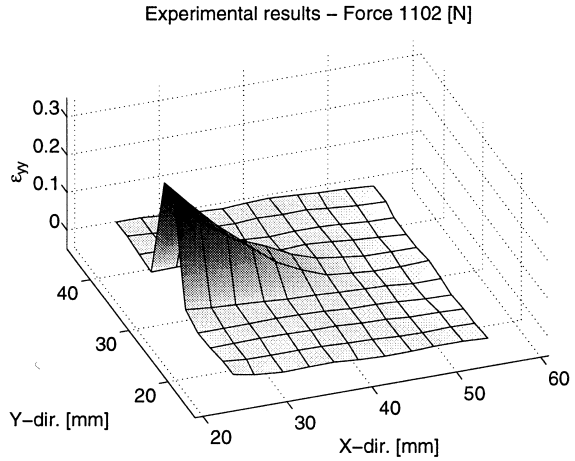

Fig. 25. Experimental ε_{yy}-strains, sample D.

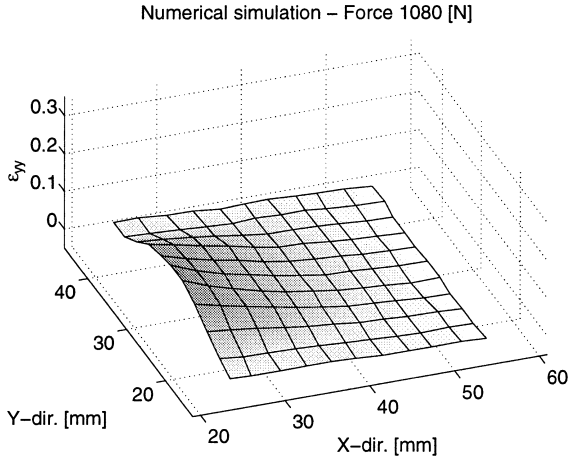

Fig. 26. Computational ε_{yy}-strains, sample D.

strain fields are given in Figs 25 and 26. The $[Y-\varepsilon_{yy}]$ projections, which better quantify the width of the localization zone, are shown in Figs 27 and 28.

The crack opening is incorrectly predicted. The peak intensities of the numerical strain field are far too small and the width of the zone with significant strains is inconsistent with the measured strain field. This simulation of the process zone thus leads to erroneous local strain fields and to wrong material parameters. The picture of the global mechanical behaviour is misleading, and does not reveal the intrinsically local (or rather nonlocal) characteristics of the damage and fracture process. A correct numerical-experimental parameter estimation process for strain localization, damage evolution or crack propagation inevitably necessitates the use of locally measured deformation data, or data which indirectly depend on the local material behaviour. It should be remarked that although the parameter κ_i in Table 2 differs slightly from the value in Table 1, it is

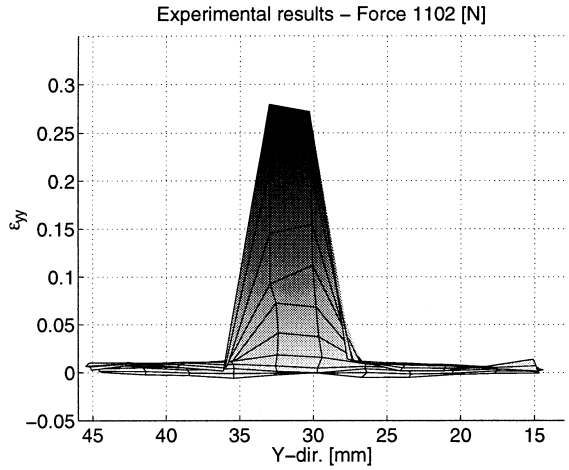

Fig. 27. Experimental ε_{yy}-strains, sample D.

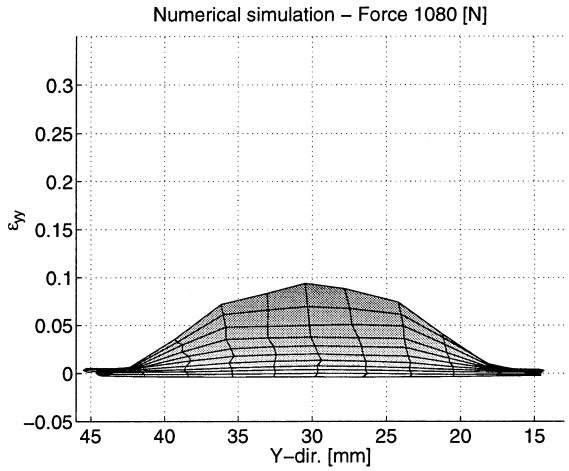

Fig. 28. Computational ε_{yy}-strains, sample D.

undoubtedly possible to find an incorrect solution with the same κ_i in both cases. It then becomes even more clear that a tensile test cannot be used to quantify the material parameters, since uniformity and stability of the damage process are rapidly lost.

Many suggestions for the determination for the nonlocal parameters of a continuum (Bažant and Pijaudier-Cabot, 1989; Pijaudier-Cabot, 1995; Carmeliet, 1997) are based on an inverse FEM-analysis of the size effect. By fitting the peak and post-peak response for different specimen sizes, the local material behaviour (which depends on an internal length scale) is indirectly investigated. On the contrary, a local analysis of the strain fields gives direct information with respect to the failure mechanism, independently of the size of the specimen.

4.5. Assessment of the damage and crack propagation

Several aspects of the deformation, damage localization and failure mechanisms can be exemplified with evolution plots. The spatial damage distribution during two stages of the crack propagation is displayed in Figs 29 and 30 for a small specimen with a characteristic dimension $W = 50$ mm and a notch depth $a_n = 10$ mm. The damage field has been computed with the medium mesh in Fig. 10. The loading force and the relative displacement of the loading pins in each stage is given on the figures. The completed damage band spreads over several elements and has an average width of a few millimetres. In the damaged zone, fibre-matrix debonding, fibre pull-out, fibre fracture and microcracking of the polypropylene matrix occur.

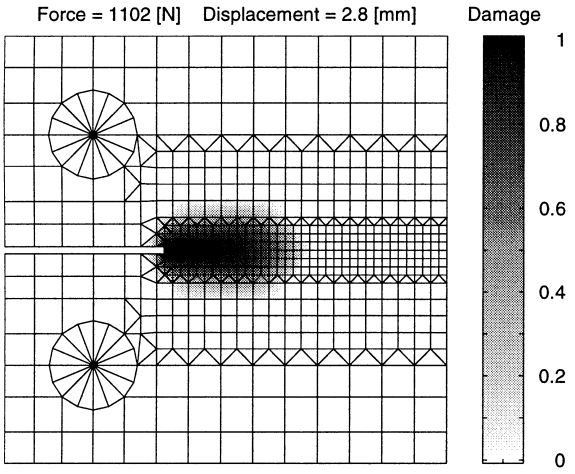

Fig. 29. Onset of damage.

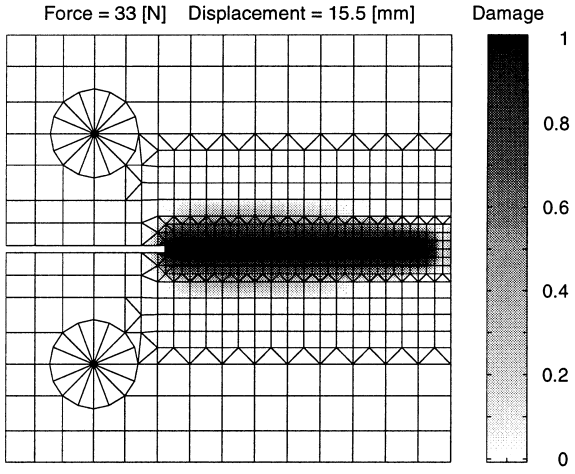

Fig. 30. Final damage distribution.

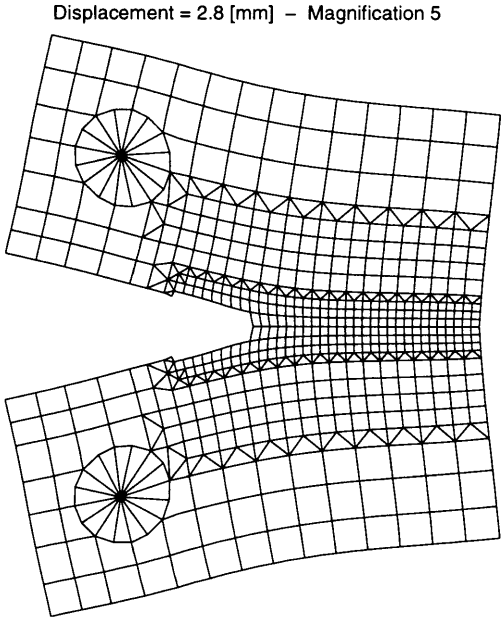

Fig. 31. Onset of crack propagation.

The deformation of the specimen and the crack propagation in two samples are represented in Figs 31 and 32. The fully damaged elements have been removed in these representations, resulting in a realistic image of the crack evolution in the CT-test. Figure 32, displayed with unscaled displacements, clearly illustrates the capability of simulating significant crack openings.

5. Conclusions

Global force-displacement curves and experimentally determined strain fields from Compact-Tension experiments on short glass-fibre-reinforced polypropylene (SGFPP) have been used to carry out a parameter quantification with a strain-based transient-gradient damage approach. Some preliminary phenomenological observations regarding the failure behaviour of SGFPP have been made, and the nonlocal character of the failure process has been emphasized. A good understanding of all failure characteristics and the associated parameters significantly reduces the number of iterations in the quantification procedure. A good agreement between theory and experiments has been established.

The necessity and the importance of a local comparison (e.g. by using local strain fields) has been motivated and discussed and the consequences of an incorrect value of the internal length parameter have been illustrated. It has been shown that a parameter estimation and verification based on the global mechanical response only, may lead to an erroneous prediction of the nonlocal interaction in the process zone. Of course, the global load-displacement curve must be fitted correctly, but this does not guarantee the proper determination of the nonlocal parameters. The

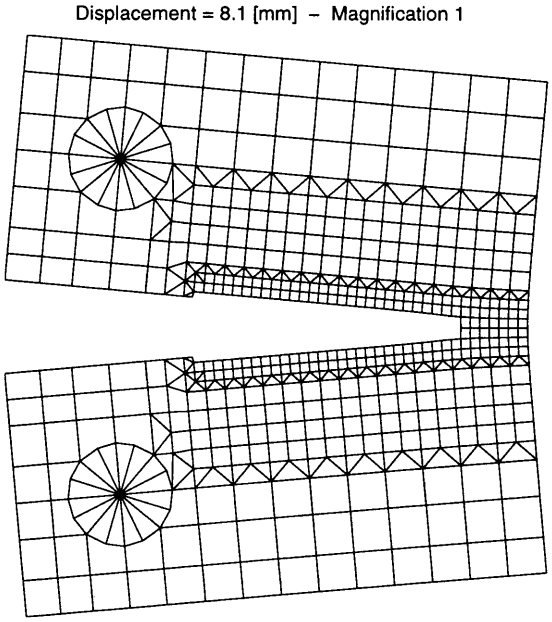

Fig. 32. Fully cracked specimen.

local verification of the strain fields provides a comparison which is more relevant with respect to the underlying mechanical processes which lead to damage and failure. The verification of this local behaviour provides a new possibility to determine the nonlocal parameters of a continuum, which is more accurate than the inverse computational modelling of the experimentally observed size effect.

References

Bažant, Z.P., Pijaudier-Cabot, G., 1989. Measurement of characteristic length of nonlocal continuum. J. of Eng. Mech. 115, 755–767.

Carmeliet, J., 1997. Inverse identification of gradient damage parameters from localization phenomena in quasi-brittle materials. In: Owen, D.R.J., Onate, E., Hinton, E., (Eds), Computational Plasticity, Fundamentals and Applications, Proceedings of COMPLAS V, Barcelona, CIMNE, pp. 798–803.

Czigány, T., Karger-Kocsis, J., 1993a. Comparison of the failure mode in short and long glass fiber-reinforced injection-molded polypropylene composites by acoustic emission. Poly. Bull. 31, 495–501.

Czigány, T., Karger-Kocsis, J., 1993b. Determination of the damage zone size in textile fabric reinforced polypropylene composites by loading the acoustic emission. Poly. and Poly. Comp. 5, 329–339.

de Borst, R., Geers, M.G.D., Sluys, L.J., 1997a. On parameter estimation in damaging solids. In: Hendriks, M., Jongdijk, H., Rots, J., van Spanje, W., (Eds.), Proceedings of the Second International Diana Conference on Computational Mechanics, DIANA, Balkema, Rotterdam, pp. 343–350.

de Borst, R., Pamin, J., Peerlings, R.H.J., Sluys, L.J., 1995. On gradient-enhanced damage and plasticity models for failure in quasi-brittle and frictional materials. Computat. Mech. 17 130–141.

de Borst, R., Sluys, L.J., Mühlhaus, H.B., Pamin, J., 1993. Fundamental issues in finite element analyses of localization of deformation. Eng. Computat. 10, 99–121.

de Borst, R., Wang, W.M., Geers, M.G.D., Sluys, L.J., 1997b. Material instabilities and internal length scales. In: Owen, D.R.J., Onate, E., and Hinton, E., (Eds.), Computational Plasticity, Fundamentals and Applications, Proceedings of COMPLAS V, CIMNE, pp. 56–71.

Frémond, M., Nedjar, B., 1996. Damage, gradient of damage and principle of virtual power. Int. J. of Sol. and Struct. 33, 1083–1103.

Geers, M.G.D., 1997. Experimental Analysis and computational Modelling of Damage and Fracture. PhD thesis, Eindhoven University of Technology, The Netherlands.

Geers, M.G.D., de Borst, R., Brekelmans, W.A.M., 1996a. Computing strain fields from discrete displacement fields in 2d-solids. Int. J. of Solids and Struct. 33, 4293–4307.

Geers, M.G.D., de Borst, R., Brekelmans, W.A.M., Peerlings, R.H.J., 1998. Strain-based transient-gradient damage model for failure analyses. Comp. Methods in App. Mech. and Eng. 160 (1–2), 133–154.

Geers, M.G.D., Peijs, T., Brekelmans, W.A.M., de Borst, R., 1996b. Experimental monitoring of strain localization and failure behaviour of composite materials. Composites Science and Tech. 56, 1283–1290.

Gibson, A.G., Manson, J.-A., 1992. Impregnation technology for thermoplastic matrix composites. Composites Manufac. 3, 223–233.

Hine, P.J., Duckett, R.A., Ward, I.M., Allan, P.S., Bevis, M.J., 1996. Comparison of short glass fiber reinforced polypropylene plates made by conventional injection molding and using shear controlled injection molding. Poly. Composites 17, 400–407.

Hugo, J., Sova, M., Čižinský, J., 1993. Creep and creep damage of glass fibre reinforced polypropylene. Composite Struc. 24, 233–244.

Kachanov, L.M., 1958. Time of the rupture process under creep conditions. Tzv. Akad. Nauk. SSR. Otd. Tekh. 8, 26–31.

Karger-Kocsis, J., 1993. Instrumented impact fracture and related failure behavior in short- and long-glass-fiber-reinforced polypropylene. Composites Science and Tech. 48, 273–283.

Karger-Kocsis, J., Fejes-Kozma, Z., 1994. Failure mode and damage zone development in a GMT-PP by acoustic emission and thermography. J. of Reinforced Plastics and Composites 13, 768–792.

Karger-Kocsis, J., Harmia, T., and Czigány, T., 1995. Comparison of the fracture and failure behavior of polypropylene composites reinforced by long glass fibers and by glass mats. Composites Sci. and Tech. 54, 287–298.

Mazars, J., Pijaudier-Cabot, G., 1989. Continuum damage theory—application to concrete. J. of Eng. Mech. 115, 345–365.

Mühlhaus, H.B., de Borst, R., Sluys, L.J., Pamin, J., 1994. A thermodynamic theory for inhomogeneous damage evolution. In: Siriwardane, H.J., Zaman, M.M., (Eds.), Comp. Methods and Advances in Geomech. Balkema, Rotterdam and Boston, pp. 635–640.

Peerlings, R.H.J., de Borst, R., Brekelmans, W.A.M., de Vree, J.H.P., 1996a. Gradient-enhanced damage for quasi-brittle materials. Int. J. for Numer. Methods in Eng. 39, 3391–3403.

Peerlings, R.H.J., de Borst, R., Brekelmans, W.A.M., de Vree, J.H.P., Spee, I., 1996b. Some observations on localisation in non-local and gradient damage models. Euro. J. of Mech., Part A/Solids 15, 937–953.

Peerlings, R.H.J., de Borst, R., Brekelmans, W.A.M., Geers, M.G.D., 1997. Gradient-enhanced damage modelling of concrete fracture. Mech. of Cohesive-Frict. Mater. Accepted.

Pijaudier-Cabot, G., 1995. Non-local damage. In: Mühlhaus, H.B., (Ed.), Continuum Models for Materials with Microstructure, Chap. 4, John Wiley & Sons Ltd, pp. 105–143.

Williams, J., Cawood, M., 1990. European group on fracture: K_c and G_c methods for polymers. Polymer Testing, 9, 15–26.

Zamzow, H., 1990. The Hentschel Random Access Tracking System HSG 84.30. In: SPIE, vol. 1356, pp. 130–133.